Agrociencia

ESTIMATION OF LAND COVER CHANGE USING LANDSAT SATELLITE IMAGERY AND THE RANDOM FOREST CLASSIFIER

José **Rodríguez-Rosales**[1], Juan Manuel **González-Camacho**[1*], Antonia **Macedo-Cruz**[2], Yolanda M. **Fernández-Ordoñez**[1]

[1]Colegio de Postgraduados Campus Montecillo. Posgrado en Socioeconomía, Estadística e Informática-Cómputo Aplicado. Carretera México-Texcoco km 36.5, Montecillo, Texcoco, State of Mexico, Mexico. C. P. 56264.
[2]Colegio de Postgraduados Campus Montecillo. Posgrado en Hidrociencias. Carretera México-Texcoco km 36.5, Montecillo, Texcoco, State of Mexico, Mexico. C. P. 56264.
* Author for correspondence: jmgc@colpos.mx

Citation: Rodríguez-Rosales J, González-Camacho JM, Macedo-Cruz A, Fernández-Ordoñez YM. 2024. Estimation of land cover change using Landsat satellite imagery and the random forest classifier. **Agrociencia.** https://doi.org/ 10.47163/agrociencia.v58i8.2846

Editor in Chief:
Dr. Fernando C. Gómez Merino

Received: July 13, 2022.
Approved: November 12, 2024.
Published in Agrociencia: December 20, 2024.

ABSTRACT

The quantification of land cover change facilitates natural resource management. In general, these changes are determined at large scales but less frequently at a regional level. In this research, changes in land area covered by vegetation (*V*), agricultural use (*A*), grassland (*G*), and urban-rural (*U*) were estimated for the period 2002–2021 in the municipality of Huehuetla, in the Northern Sierra of Puebla, Mexico (39.5 km^2), based on Landsat satellite images and the random forest classifier (RF). The latter was trained and evaluated with two datasets consisting of three spectral bands (red, green, and blue) and seven vegetation indices. RF performed well in classifying the four cover types at the beginning and end of the evaluation period. RF obtained an overall correct classification accuracy of 92.5 % in 2002 and 92.3 % in 2021. At the land cover level, RF identified vegetation cover with an F1 score of 100 % in 2002 and 98.2 % in 2021; however, it identified the urban-rural cover less effectively, with an F1 of 71.5 % in 2002 and 81.8 % in 2021. In the period analyzed, the urban area increased from 1.7 to 6.4 % (an increase of 4.7 % of the total area), and the vegetation area from 48.1 to 68.7 % (an increase of 15.6 %), at the expense of a reduction in the grassland area (19.8 %), while the agricultural area remained stable (reduction of 0.5 %). This study illustrates the importance of using machine learning techniques and satellite images to assess land cover changes at the regional level as a viable and low-cost alternative.

Keywords: Machine learning, decision trees, land use, natural resources, resource management.

INTRODUCTION

The integrated management of natural and environmental resources represents one of the central problems in the development of communities in the Northern Sierra of the state of Puebla, Mexico. Changes in land use and vegetation reflect the transformation of the environment because of the interaction of natural and human factors (Guevara-Romero and Montalvo-Vargas, 2015). Loera-Martínez *et al*. (2017) pointed out that

coffee cultivation is the main activity that generates income for smallholders in the region; however, the coffee crisis in the 1990s led to the development of cattle ranching in the area, and new pastures were opened in areas of forest and perennial or annual crops. The municipality of Huehuetla, Puebla, is geographically divided into two main areas: one with an area of 39.5 km² (studied area) and the other with 8.1 km² (INEGI, 2010), which distribute their land use in agriculture (52.6 %), urban area (1.6 %), grassland (33.9 %), jungle (11.5 %), and forest (0.38 %).

Ardila-López et al. (2005) reported that in the 1990s, satellite image classification and analysis models included classical statistical techniques such as maximum likelihood or minimum distance classification; however, these methods have low accuracy for solving problems that are nonlinearly separable between classes. In contrast, Eisavi *et al*. (2015) reported the use of the random forest (RF) model to estimate land cover change from digital images, with an overall classification accuracy of 95.1 %. Similarly, Baeza *et al*. (2014) obtained an overall accuracy of 89.6 % in the classification of four land covers (perennial forage resources, afforestation and bush, summer crops, and double cropping) in Uruguay, based on decision trees, normalized difference vegetation index (NDVI-MODIS) time series in the period from May 2011 to March 2012, and Landsat satellite images.

In Spain, Paredes-Gómez *et al*. (2019) reported the monitoring and evaluation of irrigated arable crops from Sentinel 2 satellite imagery and decision trees from 2016 to 2018, with an overall classification accuracy of 84, 79.5, and 83.7 %, respectively, in the three years of study. Chucos-Baquerizo and Vega-Ventocilla (2022) conducted a study in the Peruvian Amazon to evaluate four land covers (water bodies, crops, urban, and forests) based on three machine learning algorithms from Landsat 8, Sentinel 2 multispectral satellite images (support vector machine, SVM), and Bayes-naive, and obtained an accuracy of 90.9 % and RF of 86.4 %. The RF classifier is an efficient and simple method that has been successfully used in forest species mapping (Chuvieco-Salinero, 2010).

The objective of this study was to evaluate changes in vegetation cover and land use in the period from 2002 to 2021 in the municipality of Huehuetla, in the Northern Sierra of Puebla, Mexico, by means of a comparative analysis of Landsat images classified with the RF classifier.

MATERIALS AND METHODS

Image collection

The Landsat 7 images (LE07_L1TP_025046_20020115_20170201201_01_T1), acquired on January 15, 2002, and Landsat 8 images (LC08_L1TP_025046_20211229_20220106_01_T1) from December 29, 2021, were obtained from the United States Geological Survey (USGS) website. Both images have a spatial resolution of 30 m, and the panchromatic band has a spatial resolution of 15 m (USGS, 2019). The images were

obtained in the original sensor format, which is known as product level 1 (L1), without any preprocessing. The images were selected in such a way that they did not present cloudy conditions in the study area. The municipality files were downloaded in shapefile format from the Geo Information 2021 portal of the National Biodiversity Information System (CONABIO, 2021).

Computer resources

The creation of a database of samples of the types of soil cover existing in the study area, based on color characteristics, was carried out in the Python 3.10 programming language and the Scikit-learn machine learning software library. The computer hardware used in the image preprocessing was a Lenovo Ideapad 320 with a Windows 11 operating system, AMD A12-9720P RADEON R7 processor, 12 compute cores 4C+8G, 2.7 GHz, a 1 Tb hard disk, and 12 Gb RAM. Training and validation of the model were carried out on the Google Collaboratory Service platform to take advantage of high-performance computational resources.

Image processing

Image processing was performed with the freely available QGIS desktop 3.24.1 software and its add-on (SCP, semi-automatic classification plugin) (Congedo, 2016). In this research, the following satellite image processing steps were applied (Hantson *et al*., 2011):

Geometric correction

A geometric correction was made to each Landsat image to assign to each pixel the UTM coordinates corresponding to the UTM coordinate reference system WGS84 zone 14N. The images provided by the USGS were georeferenced with the QGIS software.

Atmospheric correction

Atmospheric correction was performed to eliminate the scattering and absorption effect of the atmosphere and to obtain the surface reflectance in the image using the dark object subtraction method of the QGIS software based on the image. This allowed improving the visual quality of the satellite image and eliminating the intrusive components of the atmosphere.

Pansharpening

This procedure combines information from the red, green, and blue (RGB) spectral bands and the panchromatic band. As a result, a multispectral image was obtained with the RGB bands with 15 m spatial resolution of the panchromatic band; for this, a Brovey transformation was applied based on intensity values of the bands (Congedo, 2016).

Histogram equalization

This procedure generates a uniform distribution of pixels in the image to improve the contrast of the satellite images to appreciate the details. The routines available in the Scikit-image library were applied according to the methodology described by Dey (2020). The correction was applied individually to each chromatic channel to obtain an image with optimized local contrast.

Processed Landsat images

Landsat images were cropped to the size of the municipality of Huehuetla and exported to jpg format for color feature extraction (Figure 1).

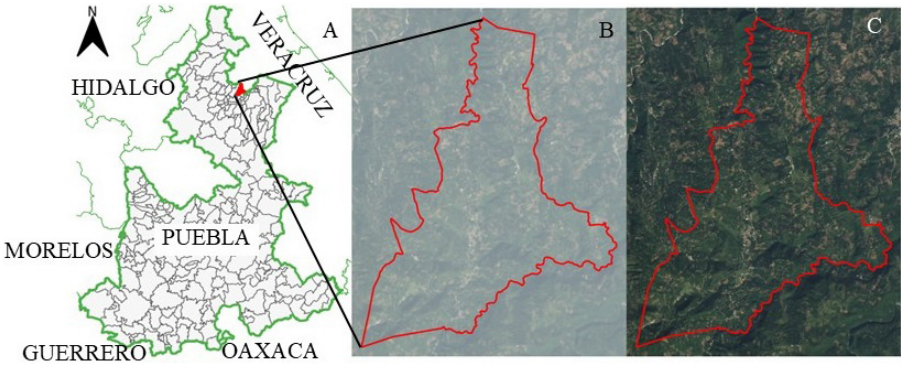

Figure 1. Combination of RGB bands from Landsat 8 satellite image in 2021. A: Location of the municipality of Huehuetla, in the northern Sierra of Puebla, Mexico; B: Landsat 8 image without corrections (spatial resolution 30 m); C: Landsat 8 image with geometric, atmospheric, and pansharpening corrections (spatial resolution 15 m).

Satellite image sampling

Image samples for each land cover and land use class were obtained using the region selection algorithm, which consists of extracting the three RGB spectral color bands of each pixel and their location coordinates (x, y) in the image. The region selection algorithm allows selecting an initial seed pixel and then comparing nearby (neighboring) pixels by means of a similarity criterion. The success of the extraction depends on the similarity criterion and the selection threshold (Valdés *et al*., 2015).

The selection of a seed pixel for each cover category was made based on information from the shapefile format of land use and vegetation of series I (INEGI, 2001) and VII (INEGI, 2021) of the geographic metadata catalogs containing vegetation cover, human settlements, grassland, and agricultural areas. These files were contrasted with the images to allow the identification of each cover category and to determine the precise location of the seed pixels.

After extracting similar pixels in each target class, four subsets of sample data were created corresponding to the target classes: agricultural (*A*), grassland (*G*), vegetation (*V*), and urban-rural (*U*). The total set of extracted pixel samples was processed to remove repeated samples within classes and then between classes to obtain an input dataset with three features or predictor variables of RGB spectral color bands associated with their corresponding target classes.

Vegetation indices

Vegetation indices are combinations of spectral bands. They are used as proxies to estimate the "greenness", density, vigor, or health status of vegetation based on its spectral response. Attenuated with other components such as soil, vegetation development is estimated by radiation intensity values (Mayorga-Arias *et al*., 2019). The seven vegetation indices used in this research were calculated based on the RGB spectral bands of Landsat satellite images (Table 1).

Input datasets

Input datasets E2002 and E2021 were created as a result of image sample extraction and calculation of vegetation indices. Each set consisted of 10 predictor variables from

Table 1. Vegetation indices calculated based on red (R), green (G), and blue (B) spectral bands.

Vegetation index	Formula
Excess green (ExG)	$E \times G = 2G - R - B$ (Ribeiro *et al*., 2005)
Excess red (ExR)	$E \times R = 1.4\ R - G$ (Meyer *et al*., 1998)
Difference between green and red excess (ExGR)	$E \times GR = exG - exR$ (Meyer and Neto, 2008)
Vegetation index extraction (CIVE)	$CIVE = 0.44R - 0.81G + 0.39B + 18.79$ (Kataoka *et al*., 2003)
Vegetative (VEG)	$VEG = \frac{G}{R^a B^{1-a}} con\ a = 0.667$ (Hague *et al*., 2006)
Normalized green-red difference (NGRDI)	$NGRDI = \frac{G - R}{G + R}$ (Gitelson *et al*., 2002)
Normalized difference (NDI)	$NDI = \left(\frac{G - R}{G + R} + 1\right) * 128$ (Gitelson *et al*., 2002)

three spectral bands (red, green, and blue) and seven vegetation indices calculated from these bands and was used to train and test the random forest classifier. E2002 consisted of 7370 observations, grouped into four target classes: *A* (1773), *G* (1653), *V* (3093), and *U* (851). E2021 consisted of 10 143 observations grouped into four target classes: *A* (2672), *G* (2246), *V* (3507), and *U* (1718).

Random forest classifier

The random forest (RF) classifier is an ensemble model that consists of calculating the average response of multiple decision trees to reduce the variance of individual trees to obtain better predictive performance and avoid the overfitting of the model (Breiman, 2001). The algorithm selects observations or replacement samples from the training set. Then, a decision tree grows with a subset of features or variables that are randomly selected. After training the decision trees, the prediction of a target class is performed with the majority vote.

The model seeks to minimize an impurity measure such as the entropy criterion or the Gini impurity criterion. The entropy criterion $I_E(t)$ for non-empty target classes is defined as:

$$I_E(t) = -\sum_{i=1}^{C} p(i|t) log_2\big(p(i|t)\big)$$

where $p(i|t)$ is the proportion of samples belonging to the target class i for a node t, and C is the number of classes. If all samples at a node belong to the same class, the entropy value $I_E(t) = 0$, but if there is a uniform class distribution, there is maximum entropy $I_E(t) = 1$.

The Gini impurity criterion $I_G(t)$ is defined as:

$$I_G(t) = 1 - \sum_{i=1}^{C} p(i|t)^2$$

where $I_G(t)$ reaches its maximum value ($I_G(t) = 1$) when the samples have a uniform distribution within classes (Raschka and Mirjalili, 2019).

The best RF model is obtained by means of a hyperparameter grid search and a cross-validation procedure. The most common hyperparameters of an RF model are the number of estimators or decision trees (*ne*) of the model, the node splitting criterion (*cr*), the maximum depth of decision trees (*md*), and the maximum number of input features (*mf*), which are randomly selected to split the nodes of a decision tree.

Performance metrics

To evaluate classifier performance, the metrics accuracy (*ACC*), precision (*P*), sensitivity (*S*), *F1* score, *F1-macro*, area under the ROC curve (AUC_{roc}) and area under the P-S curve ($AUC_{P\text{-}S}$) were used.

These metrics are derived from a confusion matrix that describes the performance of a classification model. This matrix contains four values: true positives (*TP*) are true responses predicted correctly; true negatives (*TN*) are negative responses predicted correctly; false positives (*FP*) are negative responses predicted as positive; and false negatives (*FN*) are positive responses predicted as negative (Table 2).

Table 2. Confusion matrix for the case of a binary classification of the random forest classifier.

		Predicted classes	
		Positive	Negative
True classes	Positive	*TP*	*FN*
	Negative	*FP*	*TN*

TP: true positives; *FP*: false positives; *FN*: false negatives; *TN*: true negatives.

ACC is defined as:

$$ACC = \frac{TP + TN}{TP + TN + FP + FN}$$

where *P* is the ratio of *TP* to total positive predictions, and is calculated by:

$$P = \frac{TP}{TP + FP}$$

S is the proportion of *TP* in relation to the total number of positive observed responses, that is:

$$S = \frac{TP}{TP + FN}$$

The *F1* score is the harmonic mean of *P* and *S*, and is defined as:

$$F1 = \frac{2\,P \times S}{P + S}$$

ACC, *P*, *S*, and *F1* take values between 0 and 1. A value close to zero indicates a low classifier performance, while a value close to one indicates high performance.

The overall *F1-macro* performance metric is the mean of the *F1* scores of each target class, and is calculated as:

$$F1\text{-}macro = \frac{1}{C}\sum_{i=1}^{C} F1_i$$

where $F1_i$ is the *F1* score of the *i*-th target class, and *C* is the total number of target classes. *F1-macro* is an appropriate metric when the target classes are unbalanced (Lipton *et al*., 2014).

For diagnosing classifier bias and variance problems, learning and validation curves were used. These curves are plotted as a graph of the *ACC* of training and validation against the number of samples of the input data. This plot shows whether the model has high variance or high bias, and whether collecting more data samples helps to reduce these problems.

The curve graph AUC_{ROC} associates the *TP* rate on the vertical axis against the *FP* rate on the horizontal axis, and each point on the curve represents a pair corresponding to a given decision level. The curve AUC_{ROC} takes values between 0 and 1; the closer to one, the better the performance of the classifier (Armesto, 2011). In binary classification, a AUC_{ROC} curve is obtained, while in multiclass classification, a AUC_{ROC} curve is obtained for each predicted class of the model.

The precision-sensitivity curve ($AUC_{P\text{-}S}$) identifies which values of *S* result in a reduction of *P* and vice versa. In an ideal model, the values of *P* and *S* are equal or very close to one. Analyzing the performance of a model using the curves AUC_{ROC} and $AUC_{P\text{-}S}$ provides more information about the performance of a classifier, especially when having unbalanced classes (Raschka and Mirjalili, 2019).

Random forest classifier training

Selection of the optimal characteristics and hyperparameters

The RF classifier was trained with the total set of 10 features. Subsets were selected based on the relative importance of the features obtained with the model (Raschka and Mirjalili, 2019). The selection of optimal hyperparameters of the RF classifier was performed by a lattice search and a cross-validation procedure with $k = 10$ folds of the training set.

The training and validation used 90 % of the total dataset. To evaluate the performance of the classifier in training, validation curves were generated showing the variation of the *ACC* metric from the training and validation sets as a function of the number of samples in the input dataset. The final model configuration was obtained by partitioning the data that generated the maximum *ACC* value after testing the possible combinations of hyperparameters (Table 3).

Table 3. Values of the hyperparameters that were combined in the grid search to obtain the best random forest model to estimate land cover change.

Model	Hiperparameter	Interval
RF	*ne*	50, 100, 120, 150, and 200
	cr	Entropy or Gini
	mf	Square root or Log_2
	md	8, 10, 11, 12, 13, 14, and 15

RF: random forest classifier; *ne*: number of estimators; *cr*: splitting criterion; *mf*: maximum number of features or input variables; *md*: maximum depth.

Predictive performance evaluation

The RF test for prediction was performed with the optimal hyperparameter set, with the full data set and cross-validation with $k = 10$ folds. In addition to *ACC*, all average RF performance metrics were obtained for each target class.

Calculation of land cover changes

The quantification of areas and rates of land cover change consisted of the detection and digital cartographic identification of vegetation and land use changes. Spatial analysis was used to evaluate land cover changes. Prediction with the optimal RF model was performed for each pixel of each satellite image delimiting the study area in both 2002 and 2021.

The agricultural target class included the area corresponding to bare soil in preparation; the grassland category included primary vegetation (herbaceous) and paddocks; the vegetation class included forests, secondary shrub vegetation, and shade crops; and the urban-rural class included the area occupied by buildings and infrastructure (highways, paved roads, houses, and streets) of the main population settlements.

RESULTS AND DISCUSSION

Selected characteristics or predictor variables

Based on the evaluation results of the importance of the characteristics or input variables with RF, five predictor variables with the highest importance were selected for the E2002 input dataset (*R, G, B, ExG*, and *VEG*). For the E2021 input dataset, the variables *R, G, B, ExR*, and *NGRD*I were selected (Figure 2).

Optimal hyperparameters and validation curves

The values of the optimal RF classifier hyperparameters selected for E2002 were *ne* = 120, *cr* = entropy, *mf* = square root, and *md* = 8. For E2021, *ne* = 200, *cr* = Gini, *mf* = log_2,

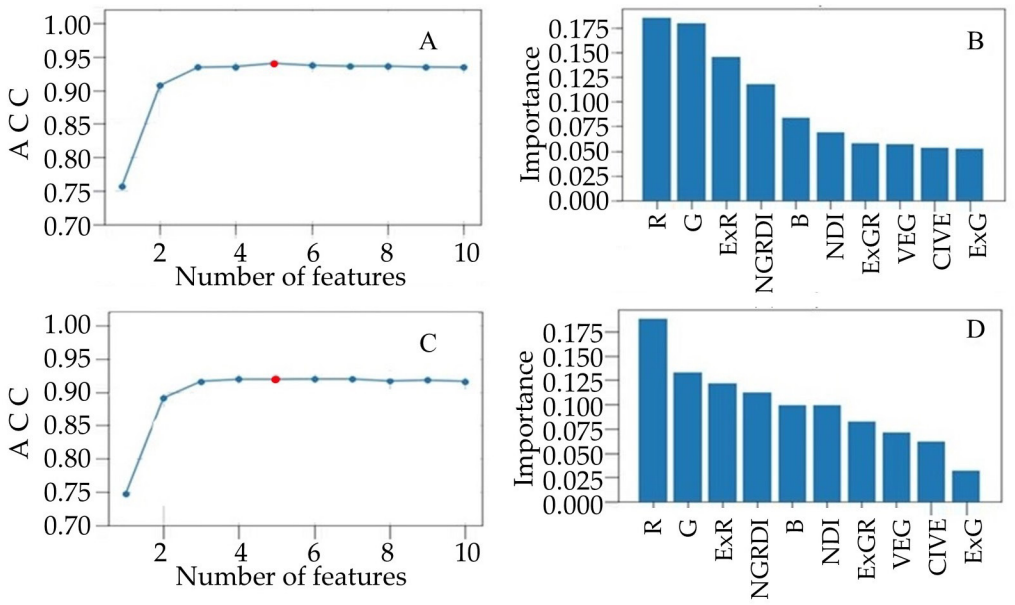

Figure 2. Optimal number and relative importance of input characteristics or predictor variables. A: E2002 performance curve; B: relative importance (E2002 scenario); C: E2021 performance curve; D: relative importance (E2021 scenario). *ACC*: accuracy; R: red spectral band; G: green spectral band; ExR: excess red; NGRDI: normalized green-red difference; B: blue spectral band; NDI: normalized difference; ExGR: difference between green and red excess; CIVE: vegetation index extraction; ExG: excess green.

and *md* = 10. The RF validation curve for E2002 showed a better fit of the data at 6000 samples, where the training and validation curves converge (Figure 3A). For E2021, the RF model was a better fit at 6500 samples, where the training and validation curves converge and stabilize (Figure 3B).

Evaluation in prediction of the random forest classifier

For the E2002 input data, RF obtained an *ACC* in prediction of 92.5 %, and for E2021, an *ACC* of 92.3 %; RF performance by target class showed that class *V* was the best ranked in both input scenarios, while class *U* was the worst ranked in terms of the F1 score metric (Table 4).

Confusion matrices

The predictive performance of RF in classifying the four target classes was analyzed with the normalized confusion matrices for scenarios E2002 and E2021. In both scenarios, class *V* was the best classified; however, RF in E2002 presented problems of confusion of class *U* with agricultural and grassland covers (classes *A* and *G*), and in E2021, it presented problems with class *A* (Figure 4).

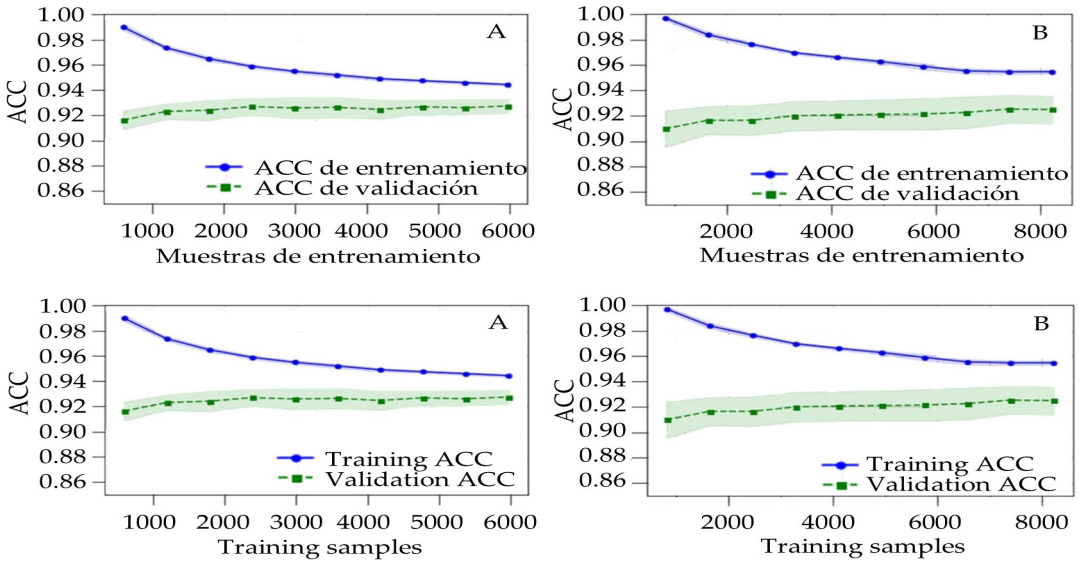

Figure 3. Learning curves of the random forest (RF) classifier for predicting target classes (agricultural, grassland, vegetation, and urban-rural). A: E2002 scenario; B: E2021 scenario. *ACC*: accuracy.

Table 4. Average prediction performance metrics of the random forest (RF) classifier for E2002 scenario and E2021 scenario.

RF	*ACC*	*F1-macro*	Class	*P*	*S*	*F1*
E2002	0.925 +/- 0.004	0.882+/- 0.006	*A*	0.898	0.898	0.898
			G	0.906	0.933	0.919
			V	1.000	1.000	1.000
			U	0.738	0.694	0.715
E2021	0.924 +/- 0.005	0.911 +/- 0.006	*A*	0.906	0.849	0.877
			G	0.969	0.960	0.965
			V	0.980	0.983	0.981
			U	0.773	0.869	0.818

A: agricultural; *G*: grassland; *V*: vegetation; *U*: urban-rural. *F1-macro* metrics: F1 global score; *P*: precision; *S*: sensitivity.

Performance curves

The receiver operating characteristic curves (AUC_{ROC}) for each target class of the RF classifier in E2002 are: class *V*, with a perfect score $AUC_{ROC} = 1$; classes *A* and *G*, with a very high score $AUC_{ROC} = 0.99$; and class *U*, with the smallest area $AUC_{ROC} = 0.97$. In the case of the classifier in E2021, classes *G* and *V* are equivalent to one, while classes *U* and *A* present an area of 0.98. However, all these values are very close to one (Figure 5). This shows that RF performed very well in both scenarios in identifying the four target classes according to this metric.

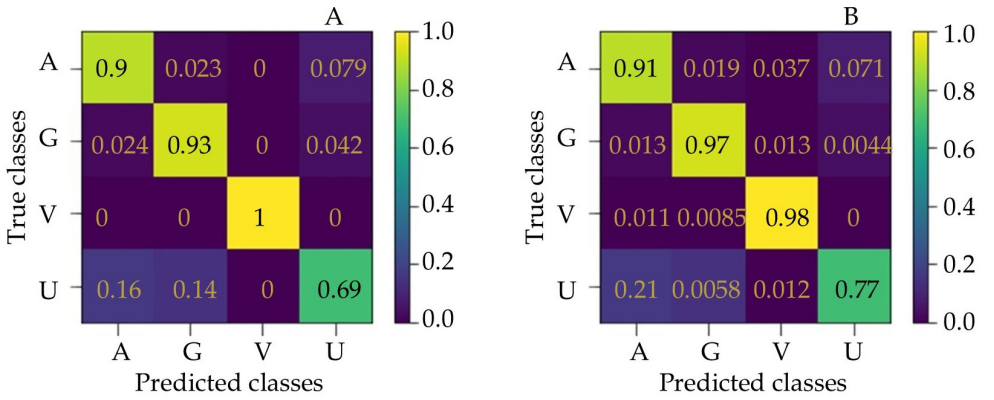

Figure 4. Normalized confusion matrix of the random forest classifier to predict agricultural (*A*), grassland (*G*), vegetation (*V*) and urban-rural (*U*) target classes. A: E2002 scenario; B: E2021 scenario.

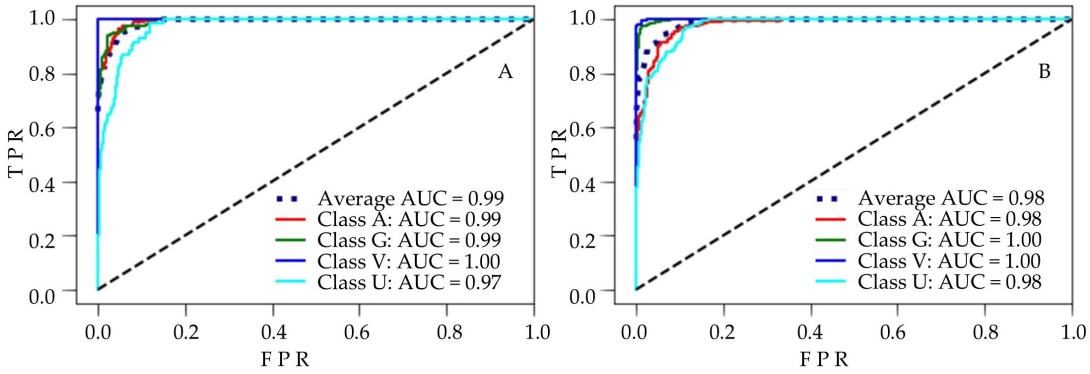

Figure 5. Random forest (RF) classifier AUC_{ROC} curves to predict agricultural (*A*), grassland (*G*), vegetation (*V*), and urban-rural (*U*) target classes. A: E2002 scenario; B: E2021 scenario. TPR: true positive rate; FPR: false positive rate; AUC: area under the curve.

The areas under the curve of precision versus sensitivity plot ($AUC_{P\text{-}S}$) show a good RF performance in identifying the target classes. In both scenarios (E2002 and E2021), RF correctly identified class *V*, and with lower performance, class *U* ($AUC_{P\text{-}S}$) = 0.83 and 0.9, respectively) (Figure 6).

The AUC_{ROC} and $AUC_{P\text{-}S}$ areas are very close to one, so the RF performance is high for classes *A*, *G*, and *V* in both input scenarios; however, class *U* presented more problems for identification. This is explained by the smaller number of data samples used to identify this class and the confusion of *U* class samples with *A* and *G* class samples (*FP*), or the reverse, *A* or *G* class samples identified as *U* class (*FN*). In unbalanced classes, the performance metric $AUC_{P\text{-}S}$ provides a more conservative estimator of classifier quality than AUC_{ROC} (Murphy, 2012).

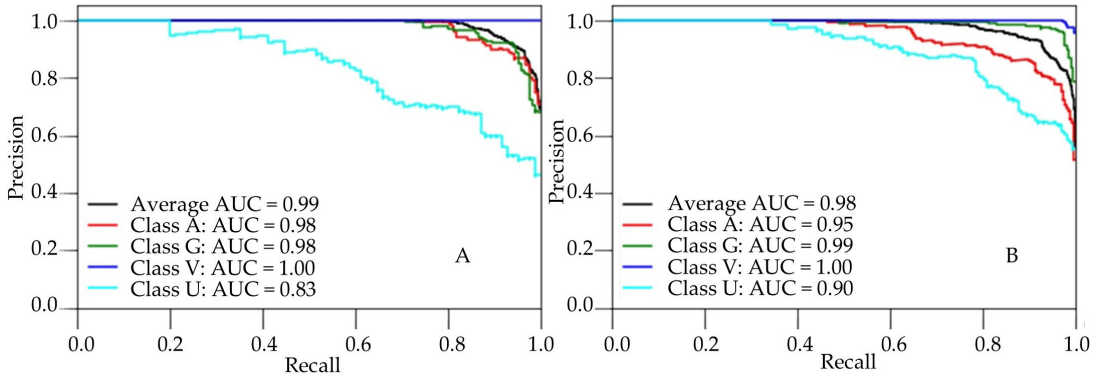

Figure 6. Accuracy-sensitivity curves ($AUC_{P\text{-}S}$) of the random forest (RF) classifier to predict agricultural (*A*), grassland (*G*), vegetation (*V*) and urban-rural (*U*) target classes; A: E2002 scenario; B: E2021 scenario. *AUC*: Area under the curve.

In this study it was not possible to obtain more pixel samples that would uniquely identify the *U* class to obtain a better balance between target classes, since in the urban-rural sector there are areas with backyards for agricultural use or grassland in the localities.

Quantification of land area and land cover change rate

With the optimal RF models for the years 2002 and 2021, a pixel classification of the images covering the study area was performed (Figure 7). During this period, an increase in class *V* and a decrease in class *G* were observed, while class *A* decreased slightly, and class *U* showed a notable increase in 2021.

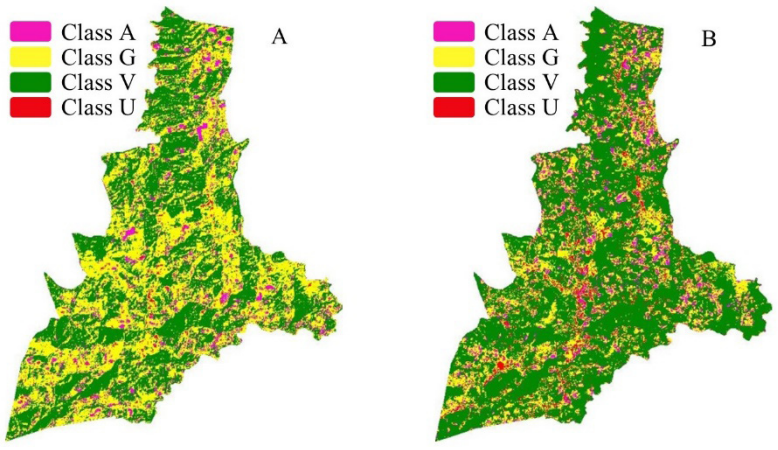

Figure 7. Land cover classification of the municipality of Huehuetla, in the Northern Sierra of Puebla, Mexico, carried out with the random forest (RF) classifier of the target classes (agricultural (*A*), grassland (*G*), vegetation (*V*), and urban-rural (*U*)). A: E2002 scenario; B: E2021 scenario.

The areas of classes *V* and *U* increased 617.3 and 186.3 ha, respectively; while classes *A* and *G* decreased 19.3 and 784.1 ha, respectively (Table 5). The decrease in areas of agricultural cover and grasslands (classes *A* and *G*) was due to their conversion to vegetation and urban-rural areas (classes *V* and *U*).

Table 5. Quantification of land cover changes (in area and relative change in relation to the total area) between 2002 and 2021 in the municipality of Huehuetla, in the Northern Sierra of Puebla, Mexico, using the random forest (RF) classifier.

Class	2002		2021		Change	
	Number of Pixels	Area (ha)	Number of Pixels	Area (ha)	Area (ha)	%
Agricultural	13 070	294.1	12 211	274.8	-19.3	-0.5
Grassland	75 064	1688.9	40 214	904.8	-784.1	-19.8
Vegetation	84 481	1900.8	111 916	2518.1	617.3	15.6
Urban-rural	3015	67.8	11 291	254.0	186.2	4.7

The increase in vegetation cover in Huehuetla is partially due to the expansion of forests and shade crops, driven by the Sowing Life Program that began in 2019 (Cotler-Ávalos *et al*., 2020). This program has promoted reforestation and the transition of agricultural and grassland areas to vegetation. In addition, an analysis by Apodaca-González *et al*. (2023) reveals that the perception of the effects of hurricanes influences the decision of producers to continue with agricultural and livestock activities. The negative impact of hurricanes such as Stan in 2005 and Dean in 2007 on the municipality's agricultural sector caused significant losses and affected the livelihoods of farmers (CENAPRED, 2009). The conversion of agricultural and grassland areas into vegetation and urban-rural zones reflects an adaptation to these environmental and socioeconomic challenges during this period.

CONCLUSIONS

The random forest machine learning classifier trained from Landsat 7 (2002) and Landsat 8 (2021) satellite images representative of the Huehuetla region, in the Northern Sierra of Puebla, Mexico, achieved an accuracy of 92.5 % in prediction to classify the four land cover types analyzed (agricultural, grassland, vegetation, and urban-rural). The most relevant features (predictors) were the red, green, and blue spectral bands in both images, as well as the excess green and vegetative plant indices for the 2002 Landsat 7 image, and the excess red and normalized green-red difference indices for the 2021 Landsat 8 image. Cover changes showed an increase in vegetation and urban-rural areas, while a decrease in agricultural and grassland areas was observed from 2002 to 2021.

REFERENCES

Apodaca-González C, Juárez-Sánchez J, Ramírez-Valverde B, Méndez-Espinoza J. 2023. Estrategias de adaptación campesina ante la variabilidad climática. Caso del café, municipio de Huehuetla, Estado de Puebla, México. Revista Geográfica Venezolana 64 (1): 73–84. https://doi.org/10.53766/rgv/2022.64.01.03

Ardila-López JP, Espejo-Valero OJ, Herrera-Escorcia JL. 2005. Validación de una metodología de clasificación de imágenes satelitales en un entorno orientado a objetos. Ingeniería 10(1): 61–69.

Armesto D. 2011. Pruebas diagnósticas: curvas ROC. Electronic Journal of Biomedicine 2011 (1): 77–82.

Baeza S, Baldassini P, Bagnato C, Pinto P, Paruelo J. 2014. Caracterización del uso/cobertura del suelo en Uruguay a partir de series temporales de imágenes MODIS. Agrociencia 18 (2): 95–105. https://doi.org/10.31285/agro.18.470

Breiman L. 2001. Random forests. Machine Learning 45 (1): 5–32. https://doi.org/10.1023/a:1010933404324

CENAPRED (Centro Nacional de Prevención de Desastres). 2009. Características e impacto socioeconómico de los principales desastres ocurridos en la República Mexicana en el año 2007. Gobierno de México. Sistema Nacional de Protección Civil. Centro Nacional de Prevención de Desastres. Ciudad de México, México. 624 p.

Chucos-Baquerizo N, Vega-Ventocilla EJ. 2022. Evaluation of machine learning algorithms in the classification of multispectral satellite images, case: Peruvian Amazon. Ciencia Latina Revista Científica Multidisciplinar 6 (1): 4946–4963. https://doi.org/10.37811/cl_rcm.v6i1.1843

Chuvieco-Salinero E. 2010. Teledetección ambiental: La observación de la Tierra desde el espacio. Digital Reasons: Ariel, España. 600 p.

CONABIO (Comisión Nacional para el Conocimiento y Uso de la Biodiversidad). 2021. Geoportal del Sistema Nacional de Información sobre Biodiversidad. http://www.conabio.gob.mx/informacion/gis/ (Retrieved: May 2021).

Congedo L. 2016. Semi-Automatic Classification Plugin: A Python tool for the download and processing of remote sensing images in QGIS. Journal of Open Source Software 6 (64): 3172. https://doi.org/10.21105/joss.03172

Cotler-Ávalos H, Manson R, Nava-Martínez JD. 2020. Evaluación de la focalización del Programa Sembrando Vida. Gobierno de México. Centro de Investigación en Ciencias de Información Geoespacial. Instituto de Ecología A.C. Consejo Nacional de Humanidades, Ciencias y Tecnologías. Ciudad de México, México. 53 p.

Dey S. 2020. Python Image Processing Cookbook: Over 60 recipes to help you perform complex image processing and computer vision tasks with ease. Packt Publishing: Birmingham, UK. 438 p.

Eisavi V, Homayouni S, Yazdi AM, Alimohammadi A. 2015. Land cover mapping based on random forest classification of multitemporal spectral and thermal images. Environmental Monitoring Assessment 187 (5): 291. https://doi.org/10.1007/s10661-015-4489-3

Gitelson AA, Kaufman YJ, Stark R, Rundquist D. 2002. Novel algorithms for remote estimation of vegetation fraction. Remote Sensing of Environment 80 (1): 76–87. https://doi.org/10.1016/S0034-4257(01)00289-9

Guevara-Romero ML, Montalvo-Vargas R. 2015. Cambio de uso de suelo y vegetación derivados de la dotación de infraestructura: Sierra Norte del Estado de Puebla. Nova Scientia 7 (13): 314–336.

Hague T, Tillet ND, Wheeler H. 2006. Automated crop and weed monitoring in widely spaced cereals. Precision Agriculture 7 (1): 21–32. https://doi.org/10.1007/s11119-005-6787-1

Hantson S, Chuvieco E, Pons X, Domingo C, Cea C, Moré G, Tejeiro JA. 2011. Cadena de pre-procesamiento estándar para las imágenes Landsat del Plan Nacional de Teledetección. Revista de Teledetección 36 (7): 51–61.

INEGI (Instituto Nacional de Estadística y Geografía). 2001. Uso del suelo y vegetación, escala 1:250000, serie I. http://geoportal.conabio.gob.mx/metadatos/doc/html/usv250s6gw.html (Retrieved: April 2022).

INEGI (Instituto Nacional de Estadística y Geografía). 2010. Compendio de información geográfica municipal 2010, Huehuetla, Puebla. Ciudad de México, México. https://www.inegi.org.mx/contenidos/app/mexicocifras/datos_geograficos/21/21072.pdf (Retrieved: April 2022).

INEGI (Instituto Nacional de Estadística y Geografía). 2021. Uso del suelo y vegetación, escala 1:250000, serie VII. Comisión Nacional para el Conocimiento y Uso de la Biodiversidad. Ciudad de México, México. http://geoportal.conabio.gob.mx/metadatos/doc/html/usv250s6gw.html (Retrieved: April 2022).

Kataoka T, Kaneko T, Okamoto H, Hata S. 2003. Crop growth estimation system using machine vision. *In* Proceedings 2003 IEEE/ASME International Conference on Advanced Intelligent Mechatronics (AIM 2003). Institute of Electrical and Electronics Engineers. Kobe, Japan. https://doi.org/10.1109/aim.2003.1225492

Lipton ZC, Elkan C, Naryanaswamy B. 2014. Optimal thresholding of classifiers to maximize F1 measure. *In* Calders T, Esposito F, Hüllermeier E, Meo R. (eds.), Machine Learning and Knowledge Discovery in Databases. ECML PKDD 2014. Lecture Notes in Computer Science 8725. Springer: Berlin, Germany. https://doi.org/10.1007/978-3-662-44851-9_15

Loera-Martínez J, Sepúlveda-Jiménez D, Sepúlveda-Robles DE. 2017. Propuesta para mejorar la productividad y rentabilidad en el medio rural del Municipio de Huehuetla, Puebla. ECORFAN 2: 1–13.

Mayorga-Arias D, Pazos-Roldán M, Uvidia-Vélez M. 2019. Uso del índice normalizado de vegetación para la elaboración de planos de cultivo. Opuntia Brava 11 (2): 261–265. https://doi.org/10.35195/ob.v11i2.760

Meyer GE, Metha T, Kocher M, Mortensen D, Samal A. 1998. Textural imaging and discriminant analysis for distinguishing weeds for spot spraying. American Society of Agricultural and Biological Engineers 41 (4): 1189–1197. https://doi.org/10.13031/2013.17244

Meyer GE, Neto JC. 2008. Verification of color vegetation indices for automated crop imaging applications. Computers and Electronics in Agriculture 63 (2): 282–293. http://doi.org/10.1016/j.compag.2008.03.009

Murphy KP. 2012. Machine learning: A probabilistic perspective. MIT Press: Cambridge MA, USA. 184 p.

Paredes-Gómez V, del Blanco-Medina V, Gutiérrez-García A, Nafría-García D. 2019. Seguimiento y evaluación de la capacidad de discriminación de cultivos herbáceos en regadío a partir de imágenes de satélite en el periodo 2016-2018. *In* Teledetección: Hacia una Visión Global del Cambio Climático. Asociación Española de Teledetección. Madrid, España, pp: 15–18.

Raschka S, Mirjalili V. 2019. Python machine learning (Third edition). Packt Publishing: Birmingham, UK. 770 p.

Ribeiro A, Fernández-Quintanilla C, Barroso J, García-Alegre MC. 2005. Development of an image analysis system for estimation of weed pressure. Precision Agriculture 2005: 169–174.

USGS (United States Geological Survey). 2019. Landsat satellite missions. United States Geological Survey. U.S. Department of the Interior. Reston, VA, USA. https://www.usgs.gov/landsat-missions/landsat-satellite-missions (Retrieved: May 2021).

Valdés SD, Mesejo LD, León MA. 2015. Selección de píxel semilla mediante wavelets para crecimiento por regiones difuso. Revista Internacional de Gestión del Conocimiento y la Tecnología 3 (1): 14–25.